

Modeling a Dual-Parallel Silicon Modulator for Sinc-Shaped Nyquist Pulse Generation

Siqi Liu , Kan Wu , *Member, IEEE*, Linjie Zhou , *Member, IEEE*, Gangqiang Zhou ,
Liangjun Lu , *Member, IEEE*, and Jianping Chen 

Abstract—Sinc-shaped Nyquist pulses have wide applications in optical communications and microwave photonics. The quality of the generated Nyquist pulses has a significant effect on the overall performance of the communication system and the signal processing system. Generating high-quality Nyquist pulses with integrated silicon modulators is however still challenging due to the highly nonlinear response and fabrication-induced discrepancies of the device. We present a model for a silicon dual-parallel modulator with which the best possible quality of the generated optical frequency comb (OFC) and sinc-shaped Nyquist pulses can be obtained. In the model, the phase and amplitude deviations are taken into consideration. Device induced waveform and spectrum distortion can be well described. Based on the guidance of the model, a root-mean-square error of 2.8% is obtained between the experimentally generated signals and the ideal pulses, which proves the high accuracy of the model and its importance for high-quality Nyquist pulse generation.

Index Terms—Silicon photonics, Nyquist pulse, Optical frequency comb, Dual-parallel modulator.

I. INTRODUCTION

SINC-SHAPED Nyquist pulses have wide applications in optical communications and microwave photonics. Sinc-shaped Nyquist pulses can be multiplexed to the zero-crossing time slots of the adjacent pulses with zero inter-symbol interference (ISI) [1], thus satisfying Nyquist zero ISI criterion. The rectangular spectrum of the sinc-shaped Nyquist pulses is known as the optical frequency comb (OFC) and shows high spectral efficiency [2]. As the demand for high-capacity optical communication grows, sinc-shaped Nyquist pulses have been intensely investigated in Nyquist transmission systems [1], [3], [4]. Sinc-shaped Nyquist pulses have also been used as the sampling pulses in the photonic analog-to-digital converter (PADC)

systems. Compared with mode-locked lasers, the traditional sampling pulse sources, sinc-shaped Nyquist pulse generation based on modulators can provide sampling sources with flexible sampling frequencies and central wavelengths, the potential to integrate on a chip, and the timing jitter comparable to active mode-locked lasers [5], [6].

The quality of the generated sinc-shaped Nyquist pulses plays an important role in the Nyquist transmission systems and the PADC systems. The non-ideal zero-crossing points of the generated Nyquist pulses may lead to ISI between adjacent pulses in optical communications. The bandwidth-limited signals can be written as the superposition of sinc-shaped Nyquist pulses [7], which means the bandwidth-limited signals can be sampled by the Nyquist pulses. Distorted Nyquist sampling pulses may lead to sampling errors and further cause wrong quantization results.

Modulation based sinc-shaped Nyquist pulse has been reported by many works [2], [8]–[12]. However, most of the reported works are based on commercial LiNbO₃ modulators with bulky size, and an integrated solution is superior due to its compact size, low cost, high power efficiency and flexibility [13]. Integrated sinc-shaped Nyquist pulse generated by silicon modulators has also been reported in recent years [5], [14], [15]. However, the quality of the generated sinc-shaped Nyquist pulses is worse than the pulses generated by LiNbO₃ modulators because the silicon modulators have worse linearity. The electro-optic (EO) modulation of the PN junctions in the silicon modulator is based on the free-carrier dispersion (FCD) effect and is nonlinear whereas the EO modulation in LiNbO₃ modulators is based on the linear Pockels effect. The fabrication errors of the silicon devices may lead to performance discrepancies of the multimode interferometers (MMIs) and the PN junctions. The response nonlinearity and the fabrication errors mentioned above can cause distortion in the generated pulses and deteriorate the general performance of the optical communication systems or the PADC systems. Thus, it is necessary to establish a model for the fabricated silicon modulators and guide the experiment to generate sinc-shaped Nyquist pulses with the best possible quality.

Modeling PN junctions of a silicon modulator has been reported [16]–[20]. In some works, the model for PN junctions is established to design the profile and doping concentration of the PN junctions so that the fabricated modulator can have better linearity [16]–[18]. Other works use the model to suppress the nonlinearity after fabrication [19], [20]. The models are mostly used to improve the linearity of the modulators and to

Manuscript received December 18, 2019; revised March 25, 2020; accepted April 21, 2020. Date of publication April 23, 2020; date of current version June 17, 2020. This work was supported in part by the National Natural Science Foundation of China under Grants 61922056, 61875122, 61705129, and 61535006, in part by the National Key Research and Development Program (2019YFB2203203, 2018YFB2201702), and in part by Shanghai Municipal Science and Technology Major Project (2017SHZDZX03). (*Corresponding author: Kan Wu; Linjie Zhou.*)

The authors are with the State Key Laboratory of Advanced Optical Communication Systems and Networks, Department of Electronic Engineering, Shanghai Jiao Tong University, Shanghai 200240, China (e-mail: siki-liu@sjtu.edu.cn; kanwu@sjtu.edu.cn; ljzhou@sjtu.edu.cn; zhougq_9@sjtu.edu.cn; luliangjun@sjtu.edu.cn; jpchen62@sjtu.edu.cn).

Color versions of one or more of the figures in this article are available online at <https://ieeexplore.ieee.org>.

Digital Object Identifier 10.1109/JSTQE.2020.2989829

further get better performance for an optical communication system. Therefore, a model and detailed systematic analysis on the silicon modulators for high-quality pulse generation has not been performed yet, which is of high importance to understand the best quality of the pulses generated by silicon modulators.

In this work, we present an analytic model for the silicon dual-parallel Mach-Zehnder modulator (DP-MZM) by considering the influence of both phase deviation and amplitude deviation. The phase deviation represents the nonlinear transfer function of the modulator and the nonlinear phase response of the PN junction versus bias voltage. The amplitude deviation represents the amplitude imbalance among the optical signals in the four arms of the DP-MZM. Both of them distort the optical spectrum and waveform. The model emphasizes the influence of amplitude deviation caused by the non-ideal MMI split ratio, the loss difference of PN junctions and strip-to-ridge waveguide transitions, which are all assumed to be ideal in our previous work [5], [21]. This more comprehensive model enables us to explain many discrepancies between the experimental data and the simulation results, such as the deterioration of flatness, increased power of high-order sidebands, and the waveform distortion in the time domain. Moreover, based on this comprehensive model, we are able to predict the best possible output spectrum and waveform with the current device. The model enables us to search for an optimum parameter set to minimize the distortion in the output spectrum and waveform. A root-mean-square (rms) error down to 2.8% is obtained between the experimentally generated pulses and the ideal Nyquist pulses while the model-predicted best rms error is 2.5%, which proves the potential of our model for high-quality generation of sinc-shaped Nyquist pulses. The paper is organized as follows. Section I is an introduction. In Section II, the analytical model of the DP-MZM is presented. In Section III, we show how the model parameters are experimentally determined. In Section IV, the experimental results of Nyquist pulse generation based on the model are provided. Section V is the conclusion.

II. ANALYTIC MODEL

It has been shown that the sinc-shaped Nyquist pulse can be generated by a DP-MZM [12]. Therefore, we focus on the modeling of a silicon DP-MZM in order to generate Nyquist pulses with the best possible quality. Fig. 1(a) shows the schematic structure of a silicon DP-MZM. The input CW light is first split into two arms by a 1×2 MMI (denoted as “MMI1”). In each arm, there is a push-pull MZM (“MZM1” and “MZM2”). Then the light in the two arms is combined by a 2×1 MMI (“MMI6”) and outputs. As shown in Fig. 1(b) which is an analytical model of the DP-MZM, there are totally 6 MMIs (“MMI1” ~ “MMI6”), 4 PN junctions (“PN1” ~ “PN4”) and 4 thermo-optic (TO) phase shifters (“PS1” ~ “PS4”).

The optical fields in the DP-MZM can be modeled as follows. The input optical field is denoted as E_{in} . Then the optical fields are given by:

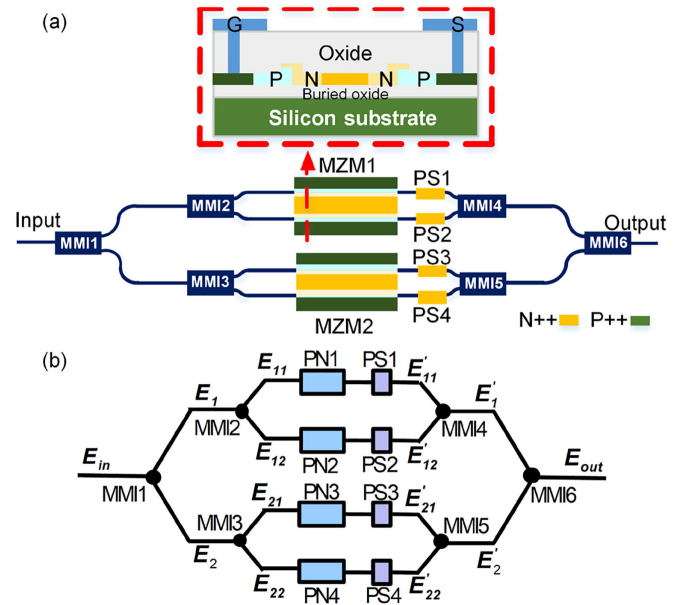


Fig. 1. (a) Schematic drawing of the DP-MZM for Nyquist pulse generation. The inset shows the cross-sectional view of active arms in the two child MZMs. (b) Analytic model of the DP-MZM.

a) Optical fields after MMI1:

$$\begin{cases} E_1 = \sqrt{s_1} E_{in} \\ E_2 = \sqrt{1 - s_1} E_{in} \end{cases} \quad (1)$$

b) Optical fields after MMI2 and MMI3:

$$\begin{cases} E_{11} = \sqrt{s_2} E_1 \\ E_{12} = \sqrt{1 - s_2} E_1 \\ E_{21} = \sqrt{s_3} E_2 \\ E_{22} = \sqrt{1 - s_3} E_2 \end{cases} \quad (2)$$

c) Optical fields after PN junctions and phase shifters:

$$\begin{cases} E'_{11} = \exp(-\alpha_1) \exp(j\varphi_{PN_bias1} + j\varphi_1) E_{11} \\ E'_{12} = \exp(-\alpha_2) \exp(j\varphi_{PN_bias2} + j\varphi_2) E_{12} \\ E'_{21} = \exp(-\alpha_3) \exp(j\varphi_{PN_bias3} + j\varphi_3) E_{21} \\ E'_{22} = \exp(-\alpha_4) \exp(j\varphi_{PN_bias4} + j\varphi_4) E_{22} \end{cases} \quad (3)$$

d) Optical fields after MMI4 and MMI5:

$$\begin{cases} E'_1 = \sqrt{s_4} E'_{11} + \sqrt{1 - s_4} E'_{12} \\ E'_2 = \sqrt{s_5} E'_{21} + \sqrt{1 - s_5} E'_{22} \end{cases} \quad (4)$$

e) Optical fields after MMI6:

$$E_{out} = \sqrt{s_6} E'_1 + \sqrt{1 - s_6} E'_2 \quad (5)$$

where the splitting ratio of MMI i is denoted as s_i ($i = 1 \sim 6$), the loss caused by the absorption of the PN junction PN i and the transitions between strip and ridge waveguides for TO phase shifters PS i is denoted as α_i ($i = 1 \sim 4$), the phase shift caused by the TO phase shifter PS i is denoted as φ_i ($i = 1 \sim 4$) and the modulation phase shift caused by the PN junction PN i is denoted as φ_{PN_biasi} ($i = 1 \sim 4$). Substituting Eq. (1) ~ Eq. (4)

into Eq. (5), the output optical field is given by

$$E_{out} = \begin{bmatrix} \sqrt{s_1 s_2 s_4 s_6} \exp(j\varphi_{PN_bias1} + j\varphi_1) \\ + \sqrt{s_1(1-s_2)(1-s_4)s_6} \\ \exp(j\varphi_{PN_bias2} + j\varphi_2) \\ + \sqrt{(1-s_1)s_3 s_5(1-s_6)} \\ \exp(j\varphi_{PN_bias3} + j\varphi_3) \\ + \sqrt{(1-s_1)(1-s_3)(1-s_5)(1-s_6)} \\ \exp(j\varphi_{PN4} + j\varphi_4) \end{bmatrix} E_{in} \quad (6)$$

$$= \begin{bmatrix} a_1 \exp(j\varphi_{PN_bias1} + j\varphi_1) \\ + a_2 \exp(j\varphi_{PN_bias2} + j\varphi_2) \\ + a_3 \exp(j\varphi_{PN_bias3} + j\varphi_3) \\ + a_4 \exp(j\varphi_{PN_bias4} + j\varphi_4) \end{bmatrix} E_{in}$$

where $a_1 = \sqrt{s_1 s_2 s_4 s_6} \exp(-\alpha_1)$, $a_2 = \sqrt{s_1(1-s_2)(1-s_4)s_6} \exp(-\alpha_2)$, $a_3 = \sqrt{(1-s_1)s_3 s_5(1-s_6)} \exp(-\alpha_3)$, and $a_4 = \sqrt{(1-s_1)s_3 s_5(1-s_6)} \exp(-\alpha_4)$. The 1×2 and 2×1 MMIs are expected to split and combine the light equally ($s_i = 0.5$, $i = 1 \sim 6$). However, the splitting ratios of the fabricated MMIs may not be exactly 0.5 and the loss factor (α_i , $i = 1 \sim 4$) of the four arms may not be the same because of the design and fabrication errors. The phase shift φ_i ($i = 1 \sim 4$) is voltage-dependent, and thus can be further expressed as $\varphi_i(V_i)$ ($i = 1 \sim 4$), V_i is the direct current (DC) voltage applied to the TO phase shifter PS_i . The modulation phase shifts φ_{PN_biasi} ($i = 1 \sim 4$) are nonlinear with the DC voltages and microwave signals applied to them because of the nonlinear EO effect (FCD) of the PN junctions. The modulation phase shift φ_{PN_biasi} ($i = 1 \sim 4$) can be expanded into third-order polynomial around the reverse bias voltage V_{PN_biasi} [19], [20]

$$\varphi_{PNi}(V_{PN_biasi} + V_{RFi}) = m_0 + m_1(V_{PN_biasi} + V_{RFi}) + m_2(V_{PN_biasi} + V_{RFi})^2 + m_3(V_{PN_biasi} + V_{RFi})^3 \quad (7)$$

where V_{RFi} is the microwave signal applied to the PN junction PN_i , m_j is the j^{th} order fitting parameter for PN junctions ($j = 1 \sim 4$).

To generate sinc-shaped Nyquist pulses, only one microwave signal is applied to one of the child MZMs, thus $V_{PN_biasi} = 0$, and $V_{RFi} = 0$ ($i = 3, 4$). The child MZM is designed based on single-drive push-pull modulation, thus the two PN junctions in the child MZM share a single reverse bias voltage ($V_{PN_bias2} = V_{PN_bias1} = V_{PN_bias}$), and are subject to opposite microwave signals ($V_{RF2} = -V_{RF1} = V_{RF}$). The experimental results shown in Section IV show that this assumption is accurate enough. Thus Eq. (6) can be further expressed as

$$E_{out} = \begin{bmatrix} a_1 \exp[j\varphi_{PN1}(V_{PN_bias} + V_{RF}) + j\varphi_1(V_1)] \\ + a_2 \exp[j\varphi_{PN2}(V_{PN_bias} - V_{RF}) + j\varphi_2(V_2)] \\ + a_3 \exp[j\varphi_3(V_3)] + a_4 \exp[j\varphi_4(V_4)] \end{bmatrix} E_{in} \quad (8)$$

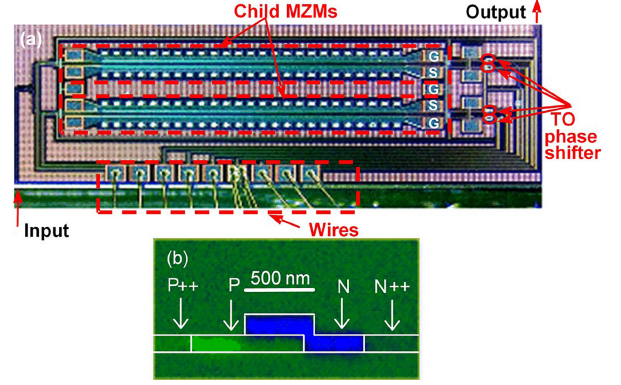


Fig. 2. (a) Optical microscope image of the DP-MZM. (b) PN junction captured by the scanning capacitance microscopy (SCM).

The output power is given by

$$I_{out} \propto |E_{out}|^2 \quad (9)$$

III. DEVICE AND PARAMETERS

In this section, we discuss how the amplitude and phase deviation parameters in the model are determined for a practical silicon DP-MZM. Amplitude deviation parameters (a_i , $i = 1 \sim 4$) can describe the amplitude imbalance between the optical signals in the four arms of the DP-MZM, and phase deviation parameters (m_i , $i = 0 \sim 3$) can describe the nonlinear phase shift of the PN junctions. The optical microscope image of the fabricated DP-MZM is shown in Fig. 2(a). The DP-MZM is consisted of passive components, such as inverse tapers and MMIs, and active components, such as PN junctions and TO phase shifters.

A. Amplitude Deviation Parameters

To obtain the amplitude deviation parameters, no microwave signals and voltages are applied to the PN junctions (i.e., $V_{RF} = 0$ and $V_{PN_bias} = 0$ in Eq. (8)). The optical field of the output signal can be expressed as

$$E_{out} = \left\{ \begin{array}{l} a_1 \exp[j\varphi_1(V_1)] + a_2 \exp[j\varphi_2(V_2)] \\ + a_3 \exp[j\varphi_3(V_3)] + a_4 \exp[j\varphi_4(V_4)] \end{array} \right\} E_{in} \quad (10)$$

By adjusting the DC voltage V_i , the phase shift $\varphi_i(V_i)$ caused by the phase shifter PS_i can be tuned from 0 to π ($i = 1 \sim 4$). When all the phase shifts are adjusted to 0, the output optical field is given by

$$E_{out0} = \left(\sum_{j=1}^4 a_j \right) E_{in} \quad (11)$$

$$\Delta P_0(dB) = 10 \log_{10} \left(\frac{E_{out0}}{E_{in}} \right)^2 = 20 \log_{10} \left(\sum_{j=1}^4 a_j \right) \quad (12)$$

$$\left(\sum_{j=1}^4 a_j \right) = 10^{\frac{\Delta P_0(dB)}{20}} \quad (13)$$

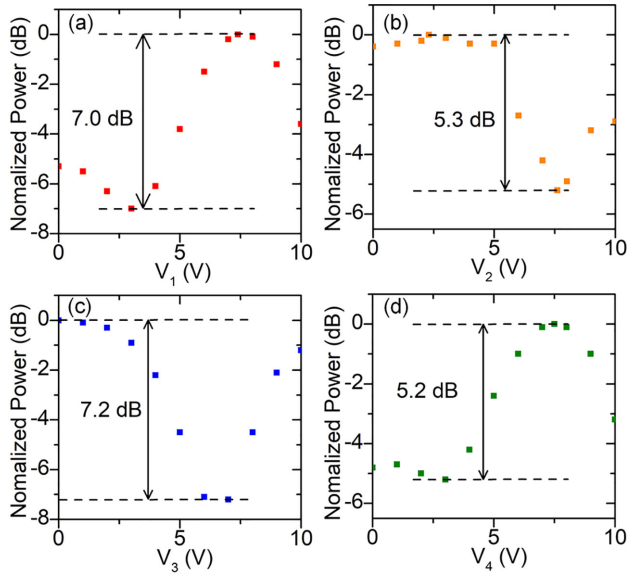


Fig. 3. Normalized measured output power versus the DC voltage V_i applied to PSi ($i = 1, 2, 3, 4$).

where ΔP_0 is the on-chip loss of the modulator, which is ~ 6 dB for the modulator used in this work. If the phase shift $\varphi_i(V_i)$ of the i^{th} phase shifter is adjusted to π ($i = 1$ or 2 or 3 or 4), while other phase shifts remain 0, the output optical field can be expressed as

$$E_{outi} = \left(\sum_{j=1}^4 a_j - 2a_i \right) E_{in} \quad (14)$$

Thus, we have

$$\Delta P_i (dB) = 10 \log_{10} \left(\frac{E_{outi}}{E_{out0}} \right)^2 = 20 \log_{10} \left(1 - 2 \frac{a_i}{\sum_{j=1}^4 a_j} \right) \quad (15)$$

$$a_i = \left(\frac{1}{2} - \frac{10^{\Delta P_i / 20}}{2} \right) \left(\sum_{j=1}^4 a_j \right) \quad (16)$$

where ΔP_i is the power difference when φ_i tuned from 0 to π and $\varphi_j = 0$ ($j = 1 \sim 4$ and $j \neq i$), as shown in Fig. 3.

The TO phase shifters are made of ridge waveguide with a width of 500 nm, a height of 220 nm, and a slab height of 90 nm. Four 50- μm -long thermo-optic (TO) phase shifters are embedded in the fabricated DP-MZM, as shown in Fig. 2(a). The MMIs are made of strip waveguides with a height of 220 nm and a width of 550 nm. Fig. 3 shows the measured power difference shown in Eq. (15). The output power in Fig. 3(b) is constant and drops only after reaching a threshold voltage. Such a condition may be caused by measurement error. However, the key parameter extracted from Fig. 3(b) is the power difference and will not be effected by this measurement error. The input CW light is set at 1550 nm and 0-dBm output power. The maximum output

TABLE I
COMPARISON OF THREE TYPES OF MODULATORS

Modulator type	Transfer function	EO effect
Ideal modulator	Linear	Linear
LiNbO ₃ modulator	Nonlinear (cosine)	Linear (Pockels effect)
Silicon modulator	Nonlinear (cosine)	Nonlinear (FCD effect)

power of the chip is about -12.0 dBm (including ~ 6.0 dB fiber coupling loss).

Using Eqs. (13) and (16), we obtain that $a_1 = 0.1356$, $a_2 = 0.1115$, $a_3 = 0.1382$, $a_4 = 0.1099$. The calculated power difference between the two arms of the child MZM with reverse bias voltage is 1.7 dB. It should be noticed that the value of $\sum a_i$ represents the total insertion loss of the modulator in Eq. (12). The value of $\sum a_i$ does not influence the amplitude deviation and the shape of the OFC and optical pulses.

B. Phase Deviation Parameters

The nonlinearity of the silicon modulators mainly comes from its nonlinear transfer function and its nonlinear EO effect. Table I compares the main difference among the ideal, LiNbO₃, and silicon modulators.

For the LiNbO₃ modulator, Eq. (8) can be rewritten as

$$E_{out} = \left\{ \begin{array}{l} a_1 \exp \left[j\pi \frac{V_{RF}}{V_\pi} + j\varphi_1(V_1) \right] \\ + a_2 \exp \left[-j\pi \frac{V_{RF}}{V_\pi} + j\varphi_2(V_2) \right] \\ + a_3 \exp \left[j\varphi_3(V_3) \right] + a_4 \exp \left[j\varphi_4(V_4) \right] \end{array} \right\} E_{in} \quad (17)$$

For our silicon DP-MZM, although the four PN junctions embedded in the modulator have identical design, the fabricated ones may have different fitting parameters shown in Eq. (7) because of the fabrication errors. Thus, the modulation phase shifts caused by the PN junctions in Eq. (7) can be further expressed as

$$\begin{aligned} \varphi_{PN1}(V_{PN_bias} + V_{RF}) &= m_{10} + m_{11}(V_{PN_bias} + V_{RF}) \\ &+ m_{12}(V_{PN_bias} + V_{RF})^2 + m_{13}(V_{PN_bias} + V_{RF})^3 \end{aligned} \quad (18)$$

$$\begin{aligned} \varphi_{PN2}(V_{PN_bias} - V_{RF}) &= m_{20} + m_{21}(V_{PN_bias} - V_{RF}) \\ &- m_{22}(V_{PN_bias} - V_{RF})^2 + m_{23}(V_{PN_bias} - V_{RF})^3 \end{aligned} \quad (19)$$

where φ_{PNi} represents the EO effect of PN_i ($i = 1, 2$) and m_{ij} ($i = 1, 2$, and $j = 0 \sim 3$).

Fig. 2(b) shows the cross-sectional image of the L-shaped PN junction measured by the scanning capacitance microscopy (SCM). With L-shaped PN junctions, the half-wave voltage of the MZMs is reduced and the modulation efficiency is improved [22], [23]. The 2.5-mm-long PN junctions are embedded in ridge waveguides. The net doping concentrations are $4 \times 10^{17} \text{ cm}^{-3}$ for the p-type region and $8 \times 10^{17} \text{ cm}^{-3}$ for the n-type region.

Fig. 4(a) and 4(c) show the normalized output power of the DP-MZM under different reverse bias voltages of the PN

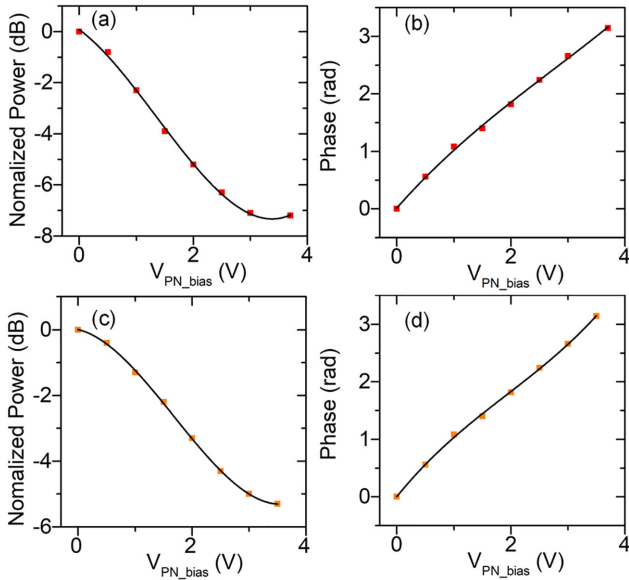


Fig. 4. (a) and (c) Measured normalized output power versus the dc voltage V_{PN_bias} applied to PN i ($i = 1, 2$). (b) and (d) The corresponding modulation phase shift of PN i versus the dc voltage V_{PN_bias} ($i = 1, 2$).

TABLE II
FITTING PARAMETERS FOR THE PN JUNCTIONS

	m_{i0}^*	m_{i1}^*	m_{i2}^*	m_{i3}^*
PN1	0.0520	1.304	-0.1626	0.0105
PN2	0.0046	1.226	-0.2398	0.0418

* $i = 1$ for PN1 and $i = 2$ for PN2.

junctions (PN1 and PN2) shown in Fig. 1(b). The modulation efficiency of the two arms is 0.925 V-cm and 0.875 V-cm respectively. Fig. 4(b) and (d) show the corresponding modulation phase shifts. The phase shifts are fit with a third-order polynomial, and the fitting parameters m_{ij} ($i = 1, 2$, and $j = 0 \sim 3$) are listed in Table II.

IV. OFC AND SINC-SHAPED NYQUIST PULSE GENERATION

In this section, we discuss the generation of high-quality Nyquist pulses based on the guidance of the proposed model. In Part A of this section, the simulated OFC and sinc-shaped Nyquist pulse generation based on three different modulators (ideal, LiNbO₃, and silicon modulators) are first compared. In Part B, the experimental results of OFC and sinc-shaped Nyquist pulse generation using a fabricated silicon DP-MZM are presented, which confirms the high accuracy of the model and its potential for high-quality Nyquist pulse generation.

A. Simulated OFC and Pulses

The ideal periodic sinc-shaped Nyquist pulses generated by an ideal modulator can be expressed as [2]

$$I(t) = |E(t)|^2 = E_0^2 \frac{\sin^2(\pi N f_m t)}{N^2 \sin^2(\pi f_m t)} \quad (20)$$

where f_m is the repetition rate of the pulses, and N is the number of OFC lines. The repetition rate is decided by the frequency of

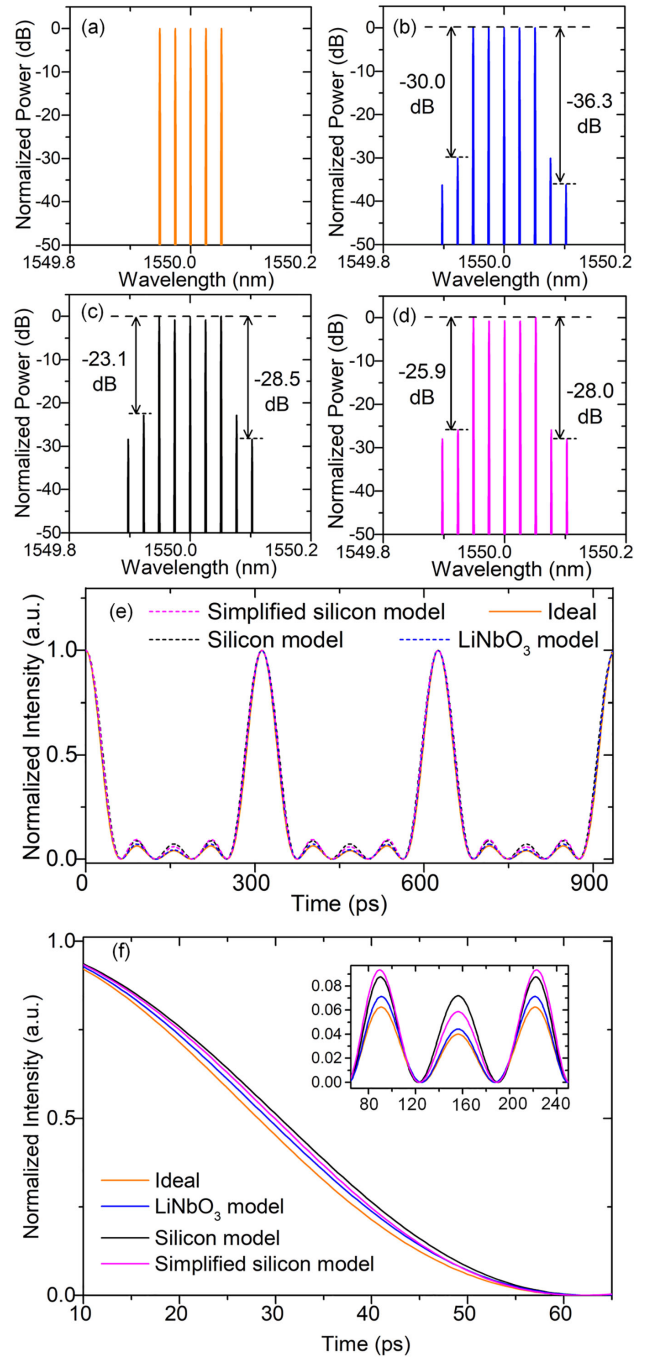


Fig. 5. Simulated optical spectrum based on (a) an ideal modulator, (b) a LiNbO₃ modulator, (c) our silicon modulator, and (d) a simplified silicon modulator, which only considers the nonlinear EO response and ignores the amplitude deviation. (e) Simulated sinc-shaped Nyquist pulses based on the ideal (orange line), LiNbO₃ (blue line), simplified silicon (magenta line) and silicon (black line) modulator. (f) Details of the simulated pulses in (e). Inset shows the small pulses of the sinc-shaped Nyquist pulses.

the applied microwave signal. In this manuscript, the repetition rate is set to 3.2 GHz. The simulated OFC lines are shown in Fig. 5(a) have a perfect rectangular optical spectrum with a flatness of 0 dB and no higher-order sidebands. The corresponding simulated theoretical pulses with a full-width at half-maximum (FWHM) duration of 56.3 ps are shown in Figs. 5(e) and 6(f).

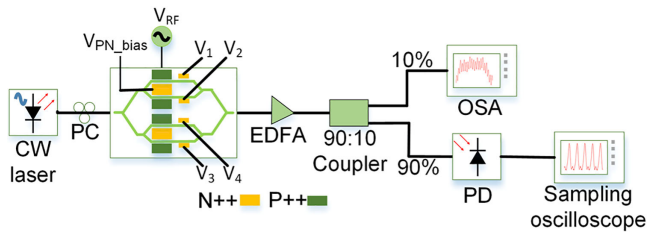


Fig. 6. Experimental setup for OFC and sinc-shaped pulse generation. OSA: optical spectrum analyzer; PD: photodiode; EDFA: erbium-doped fiber amplifier.

For sinc-shaped Nyquist pulses generated by a LiNbO_3 modulator, third- and fourth-order sidebands are generated because the cosine-shaped transfer function leads to modulation nonlinearity. The simulation is based on Eq. (17). The simulated model for LiNbO_3 modulator does not take the amplitude deviation into consideration. Fig. 5(b) shows the simulated OFC and Figs. 5(e) and 6(f) show the simulated pulses (blue lines). The simulated amplitude of the microwave signal is 1 V, and the simulated phase shift of the four TO phase shifters are $\varphi_1 = 0.07\pi$, $\varphi_2 = 1.07\pi$, $\varphi_3 = 0.85\pi$, and $\varphi_4 = 1.85\pi$. The simulated OFC has a flatness of 0 dB. The simulated suppression of the third- and fourth-order sidebands are -30.0 dB and -36.3 dB, respectively. The corresponding pulses have a larger FWHM duration of 58.4 ps compared to the theoretical pulses, as shown in Fig. 5(e). The small pulses shown in the inset of Fig. 5(f) are also higher than the theoretical ones. The rms error between the simulated pulses and ideal ones is 1.7%.

Our silicon modulator model takes both the amplitude and phase deviation into consideration. Other than the cosine-shaped transfer function, the silicon modulator also has a nonlinear EO effect (FCD effect). Thus, the nonlinearity of the silicon modulator is larger than that of the LiNbO_3 modulator. The simulation is performed by substituting Eqs. (18) and (19) into (8). The simulated amplitude of the microwave signal is 1 V, and the simulated phase shift of the four TO phase shifters are $\varphi_1 = 0.92\pi$, $\varphi_2 = 0.60\pi$, $\varphi_3 = 0.32\pi$, and $\varphi_4 = 0.29\pi$. The phase shifts are different from the phase shifts simulated in the LiNbO_3 modulator model under the same microwave signal. Fig. 5(c) shows the simulated OFC lines with a flatness of 0.8 dB. The suppression of the third- and fourth-order are worse than the OFC generated by LiNbO_3 modulator (which has a linear EO effect). The suppression of the third- and fourth-order are -23.1 dB and -28.5 dB, which are 6.9 dB and 7.8 dB higher than the sidebands of the simulated OFC using LiNbO_3 modulator model. The corresponding sinc-shaped Nyquist pulses are shown in Figs. 5(e) and 6(f) in black line. The simulated FWHM duration is 61.0 ps and the small pulses shown in the inset of Fig. 5(f) are also higher than theoretical ones and the ones simulated by LiNbO_3 modulator model. The non-ideal zero-crossing points can also be observed. The simulated pulses have an rms error of 2.5%, compared with the ideal ones.

To show the influence of the amplitude deviation, OFC and pulses generated by a simplified silicon modulator model with nonlinear EO response and without amplitude imbalance is shown in Fig. 5(d). The generated OFC has a flatness of 0.5 dB.

TABLE III
COMPARISON OF OFC AND SINC-SHAPED NYQUIST PULSES SIMULATED BY THREE TYPES OF MODULATORS

Modulator type	OFC flatness (dB)	FWHM duration (ps)	rms error*
Ideal modulator	0	56.3	0
LiNbO_3 modulator	0	58.4	1.7%
Silicon modulator	0.8	61.0	2.5%
Simplified silicon modulator	0.5	60.7	2.1%

*rms error between sinc-shaped Nyquist pulses generated by different modulators and ideal ones.

The suppression of the third- and fourth-order are -25.4 dB and -28.0 dB. The rms error between the simulated pulses based on the simplified silicon modulator model and the ideal one is 2.1%. From Fig. 5(f), it can be seen that the nonlinear EO response and amplitude deviation have comparable contribution to the waveform distortion.

B. Measured OFC and Pulses

Fig. 6 shows the setup of the experiment. The input CW light is set as 1550 nm, 0 dBm. The polarization controller is used to set the mode of the input laser to transverse electrical (TE) polarization mode because the modulator is designed to work under TE mode. The laser is then coupled to the chip through a lensed fiber. A 3.2-GHz, 22-dBm microwave signal (V_{RF}) is applied to the MZM1 shown in Fig. 1(a) by a microwave probe. A reverse bias voltage (V_{PN_bias}) of 2.9 V is applied to child modulator MZM1 to make the PN junctions work in the depletion region. Four DC voltages V_i ($i = 1, 2, 3, 4$) are applied to the four TO phase shifters. In detail, $V_1 = 1.0$ V, $V_2 = 8.3$ V, $V_3 = 4.2$ V, $V_4 = 6.8$ V. All the DC pads are wire-bonded to a printed circuit board (PCB) to apply DC voltages. The output power from the chip (about -27.5 dBm) is then divided by a 90:10 coupler. 10% of the output signal is monitored by an optical spectrum analyzer (APEX, AP2040A) for frequency-domain analysis. 90% of the signal is amplified by an erbium-doped fiber amplifier (EDFA) to ~ 0 dBm and then monitored by a 70-GHz sampling oscilloscope (Agilent DCA-X, 86100D) with a 50-GHz photodetector (u²t, XPDV2120R) for time-domain analysis.

Fig. 7(a) shows the measured OFC spectrum. The flatness of the OFC is within 1.5 dB. The suppression of the third-order and fourth-order sidebands are -22.5 dB, -23.0 dB, -27.9 dB, and -32.8 dB, which are very similar to the simulated OFC shown in Fig. 5(c). The measured sinc-shaped Nyquist pulses are shown in Figs. 7(b) and 7(c) in red line. The FWHM duration of the measured pulse is 60.3 ps, which is also close to the simulated FWHM duration of 61 ps. The rms error between the measured pulse and the simulated ones based on our silicon DP-MZM model is 1.2%. The rms error between the generated pulses and ideal Nyquist pulses is 2.8%. The rms errors show that the measured sinc-shaped Nyquist pulses are very similar

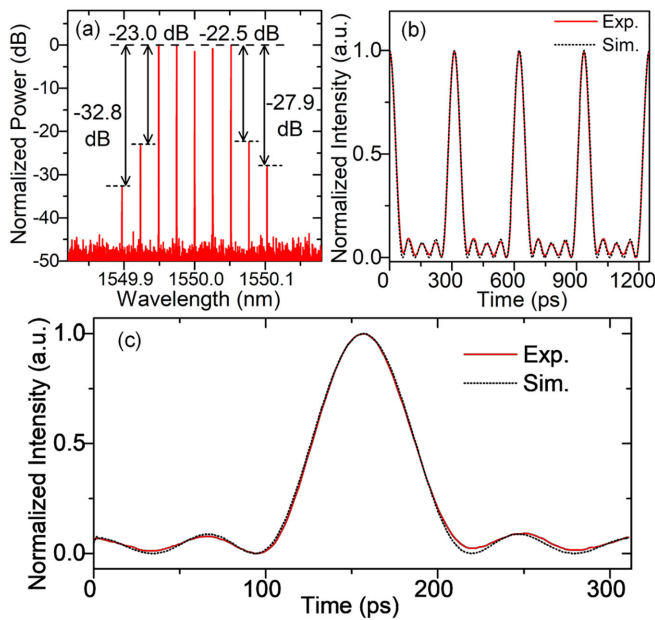


Fig. 7. (a) Measured optical spectrum. (b) Measured sinc-shaped Nyquist pulses (red line) compared with pulses simulated by the silicon modulator model (black line). (c) One period of the pulses shown in (b).

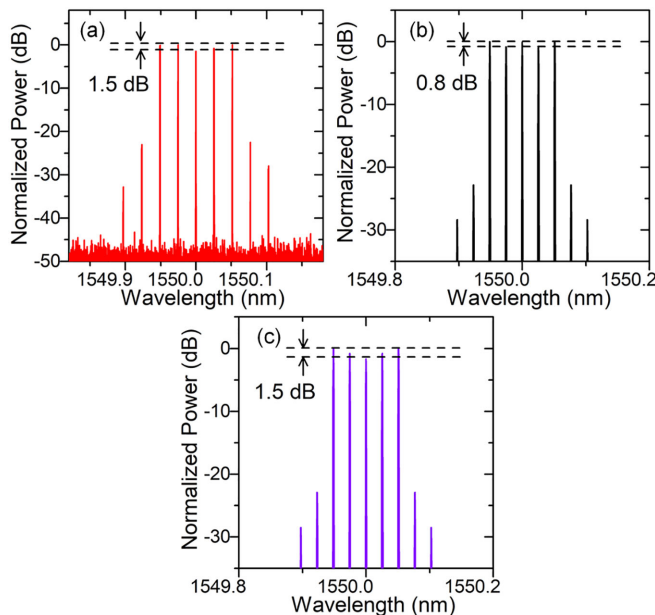


Fig. 8. (a) Measured optical spectrum and Simulated optical spectra when $\varphi_3 =$ (b) 0.3217π and (c) 0.3280π .

to the pulses of the best quality possible, and our model can provide guidance to generate sinc-shaped Nyquist pulses with high quality.

Compared to the simulated OFC which has a flatness of 0.8 dB, the measured one has a flatness of 1.5 dB. The source of the difference mainly comes from the heat instability of the TO phase shifter. It can be seen from the measured OFC in Fig. 8(a) and the simulated OFC in Fig. 8(b) that the increase of the flatness is mainly caused by the decreased power of the light carrier. Compared to the simulated OFC shown in Fig. 8(b), the

power of the light carrier of the measured OFC is decreased by ~ 0.7 dB, thus the flatness is worsened by ~ 0.7 dB. According to Eq. (8), the power of the carrier can be tuned by changing the value of φ_3 and φ_4 . The power of the carrier is decreased by ~ 0.7 dB when φ_3 in Eq. (8) changes from 0.3217π to 0.3280π (increased by $\sim 2\%$), as shown in Figs. 8(b) and (c). The phase shifts (φ_3 and φ_4) generated by TO phase shifters are sensible to the temperature in the chip, so a 2% deviation of phase shift is possible during the experiment.

V. CONCLUSION

We have established a theoretical model for a silicon DP-MZM and a systematic analysis has been performed on the high-quality pulse generation. In the model, both phase and amplitude deviations are taken into consideration. The model clearly indicates the performance difference among ideal modulators, LiNbO₃ modulators and silicon modulators. A minimum rms error of 2.8% between the generated pulse and ideal Nyquist pulse is experimentally obtained while the model predicted lowest rms error is 2.5%, which clearly proves the validity of the model and its guidance for high-quality Nyquist pulse generation.

REFERENCES

- [1] J. Zhang, J. Yu, and N. Chi, "Transmission and full-band coherent detection of polarization-multiplexed all-optical Nyquist signals generated by Sinc-shaped Nyquist pulses," *Sci. Rep.*, vol. 5, 2015, Art. no. 13649.
- [2] M. A. Soto *et al.*, "Optical sinc-shaped Nyquist pulses of exceptional quality," *Nature Commun.*, vol. 4, 2013, Art. no. 2898.
- [3] T. Hirooka, D. Seya, K. Harako, D. Suzuki, and M. Nakazawa, "Ultrafast Nyquist OTDM demultiplexing using optical Nyquist pulse sampling in an all-optical nonlinear switch," *Opt. Express*, vol. 23, pp. 20858–20866, 2015.
- [4] F. Alishahi *et al.*, "Reconfigurable optical generation of nine Nyquist WDM channels with sinc-shaped temporal pulse trains using a single microresonator-based Kerr frequency comb," *Opt. Lett.*, vol. 44, pp. 1852–1855, 2019.
- [5] S. Liu *et al.*, "Optical frequency comb and Nyquist pulse generation with integrated silicon modulators," *IEEE J. Sel. Topics Quantum Electron.*, vol. 26, no. 2, Mar./Apr. 2019, Art. no. 8300208.
- [6] V. Vercesi, D. Onori, J. Davies, A. Seeds, and C.-P. Liu, "Electronically synthesized Nyquist pulses for photonic sampling of microwave signals," *Opt. Express*, vol. 25, pp. 29249–29259, 2017.
- [7] J. Meier, A. Misra, S. Preußler, and T. Schneider, "Orthogonal full-field optical sampling," *IEEE Photon. J.*, vol. 11, no. 2, pp. 1–9, Apr. 2019.
- [8] J. Hu, S. J. Fabbri, and C. Brès, "Flexible width nyquist pulse based on a single mach-zehnder modulator," in *Proc. Conf. Lasers Electro-Opt.*, 2018, pp. 1–2.
- [9] N. Yokota, R. Igarashi, and H. Yasaka, "Optical nyquist pulse generation by using a dual-electrode Mach-Zehnder modulator," *Opt. Lett.*, vol. 42, pp. 1856–1859, 2017.
- [10] D. Wang, L. Huo, Y. Xing, X. Jiang, and C. Lou, "Optical Nyquist pulse generation using a time lens with spectral slicing," *Opt. Express*, vol. 23, pp. 4329–4339, 2015.
- [11] Y. Fang, J. Yu, J. Zhang, X. Li, N. Chi, and J. Xiao, "Frequency comb selection enabled flexible all optical nyquist pulse generation," *Opt. Commun.*, vol. 349, pp. 60–64, 2015.
- [12] J. Wu *et al.*, "Investigation on Nyquist pulse generation using a single dual-parallel Mach-Zehnder modulator," *Opt. Express*, vol. 22, pp. 20463–20472, 2014.
- [13] D. Marpaung, C. Roeloffzen, R. Heideman, A. Leinse, S. Sales, and J. Capmany, "Integrated microwave photonics," *Laser Photon. Rev.*, vol. 7, pp. 506–538, 2013.
- [14] Z. Wang *et al.*, "Optical frequency comb generation using CMOS compatible cascaded mach-zehnder modulators," *IEEE J. Quantum Electron.*, vol. 55, no. 6, Dec. 2019, Art. no. 8400206.

- [15] A. Misra, C. Kress, K. Singh, S. Preußler, J. C. Scheytt, and T. Schneider, "Integrated source-free all optical sampling with a sampling rate of up to three times the RF bandwidth of silicon photonic MZM," *Opt. Express*, vol. 27, pp. 29972–29984, 2019.
- [16] J. Ding, S. Shao, L. Zhang, X. Fu, and L. Yang, "Method to improve the linearity of the silicon Mach-Zehnder optical modulator by doping control," *Opt. Express*, vol. 24, pp. 24641–24648, 2016.
- [17] D. Pérez-Galacho *et al.*, "Simplified modeling and optimization of silicon modulators based on free-carrier plasma dispersion effect," *Opt. Express*, vol. 24, pp. 26332–26337, 2016.
- [18] G. Rasigade, D. Marris-Morini, M. Ziebell, E. Cassan, and L. Vivien, "Analytical model for depletion-based silicon modulator simulation," *Opt. Express*, vol. 19, pp. 3919–3924, 2011.
- [19] Y. Zhou, L. Zhou, F. Su, X. Li, and J. Chen, "Linearity measurement and pulse amplitude modulation in a silicon single-drive push-pull Mach-Zehnder modulator," *J. Lightw. Technol.*, vol. 34, no. 14, pp. 3323–3329, Jul. 2016.
- [20] A. Khilo, C. M. Sorace, and F. X. Kärtner, "Broadband linearized silicon modulator," *Opt. Express*, vol. 19, pp. 4485–4500, 2011.
- [21] S. Liu *et al.*, "Microwave pulse generation with a silicon dual-parallel modulator," *J. Lightw. Technol.*, vol. 38, no. 8, pp. 2134–2143, Apr. 2020.
- [22] K. Goi *et al.*, "Low-voltage silicon Mach-Zehnder modulator operating at high temperatures without thermo-electric cooling," in *Proc. Opt. Fiber Commun. Conf.*, 2016, Paper W2A. 23.
- [23] G. Zhou *et al.*, "Silicon Mach-Zehnder modulator using a highly-efficient L-shape PN junction," in *Proc. 9th Int. Conf. Inf. Opt. Photon.*, 2018, Art. no. 1096419.

Siqi Liu received the B.S. degree in electronic information science and technology from Xidian University, China, in 2015. She is currently a Ph.D. Candidate at the State Key Laboratory of Advanced Optical Communication Systems and Networks, Shanghai Jiao Tong University, Shanghai, China. Her research interests include silicon photonics, optical frequency comb and pulse generation.

Kan Wu (Member, IEEE) received the B.S. and M.S. degrees in electronic engineering from Shanghai Jiao Tong University in 2006 and 2009, and a Ph.D. degree in electrical and electronic engineering from Nanyang Technological University in 2013. He joined Electronic Engineering Department in Shanghai Jiao Tong University in 2013 and now he is an Associate Professor. His research interests include mode-locked fiber lasers and integrated optoelectronic devices.

Linjie Zhou (Member, IEEE) received the B.S. degree in microelectronics from Peking University in 2003. He received his Ph.D. degree in electronic and computer engineering from the Hong Kong University of Science and Technology in 2007. From 2007 to 2009, he worked as a Postdoctoral Researcher at the University of California, Davis. Currently, he is a Professor with the State Key Lab of Advanced Optical Communication Systems and Networks of Shanghai Jiao Tong University. His research interests include silicon photonics, plasmonic devices, and optical integration.

Gangqiang Zhou received the B.S. degree in school of physics and optoelectronic engineering from Xidian University, Xian, China, in 2016. He is currently working toward the Ph.D. degree with the State Key Laboratory of Advanced Optical Communication Systems and Networks, Department of Electronic Engineering, Shanghai Jiao Tong University, Shanghai, China. His research interests include silicon modulators and integrated microwave photonics.

Liangjun Lu (Member, IEEE) received the B.S. degree in optical engineering from Zhejiang University, Hangzhou, China, in 2011. He received the Ph.D. degree in electronic engineering from Shanghai Jiao Tong University, Shanghai, China, in 2016. He is currently a Tenure-Track Assistant Professor at the State Key Laboratory of Advanced Optical Communication Systems and Networks, Shanghai Jiao Tong University, Shanghai. His research interests include silicon photonics, and photonic integrated circuits.

Jianping Chen received the B.S. degree from Zhejiang University, Hangzhou, China, in 1983, and the M.S. and Ph.D. degrees from Shanghai Jiao Tong University, Shanghai, China, in 1986 and 1992, respectively. He is currently a Distinguished Professor with the State Key Laboratory of Advanced Optical Communication Systems and Networks, Department of Electronic Engineering, Shanghai Jiao Tong University. His main research interests include integrated photonic devices, photonic signal processing and precision fiber-optic time and frequency transfer. He is a Principal Scientist of the 973 Program in China.